Imaging Complex 3D Structures, Applying 3C Vector Migration to VSP Data

Jakob B.U. Haldorsen*, Leif Jahren*, Dorota Gressetvold*, Mathieu Milenkovic*, Any More Names†

ABSTRACT

By applying a vector-based 3D migration process to VSP data, we are able to generate a 3D image of the flank of a salt body, providing a significant improvement compared to traditional methods. The method allows the reconstruction of both the salt flank itself, and the sediments that tend to be truncated against the sides of the salt body. This is demonstrated by an application to a synthetic 3D dataset.

INTRODUCTION

Salt-related structures are common in many areas in the world (e.g., the Gulf of Mexico and the US Gulf Coast, offshore Brazil and West Africa). These structures are of special interest as they create pathways and traps for hydrocarbons.

Salt domes and some isolated salt bodies often have steeply inclined and complex boundaries, and the adjacent sedimentary layers are generally dragged upwards during salt movement and may reach dips up to 80-85° at the contact with the salt body. Commercial hydrocarbon accumulations have been found in the cap rock of salt domes as in the famous case at Spindletop (Gillespie, 1995), but more hydrocarbon is to be expected along the flanks of the dome at greater depths. Exploring for such traps has been hampered by the inability of the surface seismic method to image steeply dipping boundaries.

Figure 1 shows a seismic image obtained from a 3D surface seismic dataset acquired over and around a salt dome (Gerea et al., 2016). Steep boundaries are difficult to image directly with the surface-seismic method since reflections from these boundaries will tend to be down-going and will not be recorded with receivers at or near the surface. Commonly, these steep boundaries are characterized by the absence of amplitude or, under good conditions, by terminations of sub-horizontal features in images obtained from surface-seismic data. However, imaging sedimentary layers under an over-hanging salt canopy is difficult, and the termination of these even more difficult.

*READ AS, Hvalstad, Norway, †Total, Pau, France

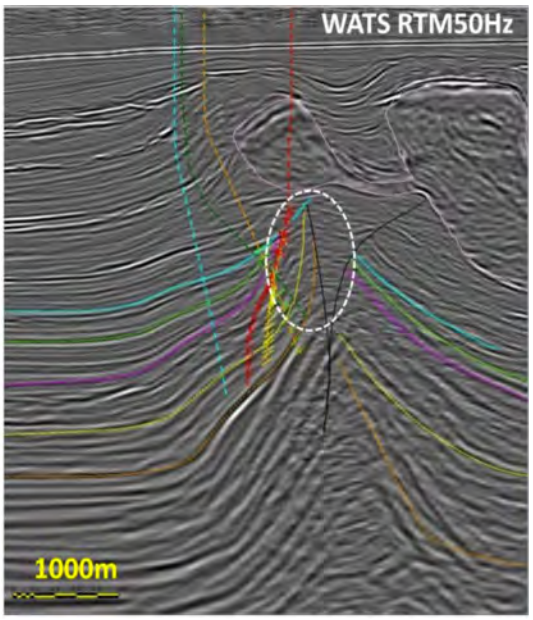

Figure 1: Seismic image obtained over a rather complex set of salt structures. The salt body shows in the upper right-hand quarter, inside a magenta-colored line. Whilst sub-horizontal sediments are clearly seen outside the salt, the structures are not well determined under the salt canopy, and it is unclear whether what we see is real or artifacts related to the salt body or complex multiples inside the salt (from Gerea et al. (2016)).

Imaging steep dips are also difficult with standard imaging techniques using down-hole receivers. However, three-component (3C) geophones deployed inside a borehole will record direct arrivals, refractions, reflections and diffractions of the wave field as it propagates away from the source and the key issue is how to use all this information in constructing an accurate image in 3D of the salt boundary.

Previous work shows how borehole seismic array tools have been used to position discrete points in 3D space that are related to the salt flank position in what is known as a salt proximity survey (SP) (Lou et al., 2012). Brooks et al. (2015) and Hal-

dorsen et al. (2015) show how vector migration can be used with zero-offset and offset VSP data to image steeply dipping structures. In this work, we apply this technique to a full 3D imaging problem.

IMAGING WITH VSP DATA

To create an image of the reflection points (Claerbout, 1985), the wave equation is used to propagate the wave field generated by the source forward in time, through a velocity model of the sediments. Similarly - in a time-reversed mode - the complete, recorded vector wave field is propagated from the receivers towards the reflector or scatterer at velocities local to the sub-surface receivers. An estimate of the strength of scattering is found as the spectral ratio of the properly normalized displacement vectors for the scattered and the incoming fields (Aki and Richard (2009), Chapter 5), i.e., by deconvolving the estimated scattered wave field by the estimated source wave field. This deconvolution enforces the coherency at the scattering point of the extrapolated source and scattered fields. In addition, a condition of synchronicity has to be applied. The two requirements of coherency and synchronicity constitute the *imaging condition* for migration. However, a spectral ratio of two wave fields tends to be unstable, and is commonly replaced by the lower-resolution correlation of the two wave fields. The two basic processes for generating images from seismic data are thus deconvolution and migration: Simply put, migration with a properly formulated imaging condition, transforms the map of reflection times to a volumetric map of formation properties.

Semblance-weighted Deconvolution

The semblance weighted deconvolution described by Haldorsen et al. (1994), is a frequency-domain least-squares process designed to find an operator $F_n^*(\omega)$ that, when applied to a data trace d_n, maximizes the bandwidth of the inverse of the signal recovered in a spatially sliding window, at the same time it minimizes the "noise". In this context, "noise" is defined at the residual after the signal, $f(\omega)$, with known arrival times, t_n, has been removed. Within a spatial window spanning $2N + 1$ traces, this problem has the analytic solution:

$$F_n(\omega) = \frac{\langle f_n^*(\omega)\rangle}{\langle E_n(\omega)\rangle}, \tag{1}$$

where the notation $\langle\cdots\rangle$ is used to mean *estimate of*, and

$$\langle f_n(\omega)\rangle = \sum_{j=n-N}^{n+N} d_n(\omega)e^{i\omega t_n} \tag{2}$$

$$\langle E_n(\omega)\rangle = \sum_{j=n-N}^{n+N} |d_n(\omega)|^2 \tag{3}$$

or the estimated signal divided by the total energy. Haldorsen et al. (1994) also show that after applying this operator, the amplitude spectrum of the signal becomes equal to the semblance spectrum, measuring the coherency of the signal estimation:

$$S_n(\omega) = \frac{|\langle f_n(\omega)\rangle|^2}{\langle E_n(\omega)\rangle}. \tag{4}$$

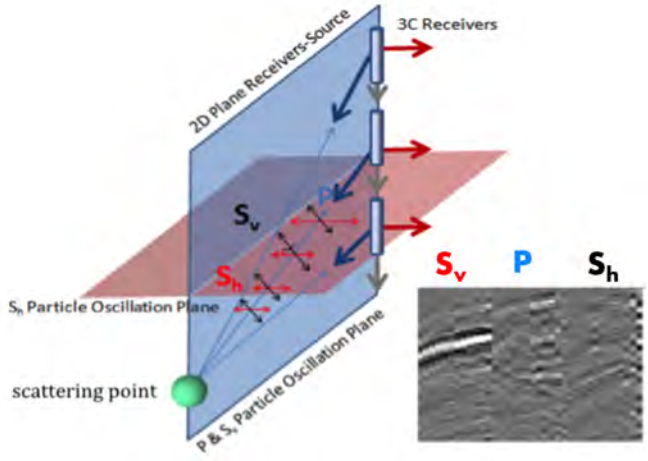

Figure 2: The elastic, scattered wave field seen by the 3C receivers (slightly modified from Haldorsen et al. (2013)).

When the signal is perfectly coherent signal, the semblance (equation 4) is equal to 1 - and equal to 0 when the signal is perfectly incoherent. Thus, the filter defined by equations 1, 2, and 3, is inherently stable, as when this filter is applied to the data, the spectra of the resulting data traces fall between the values 0 and 1.

Ray-based Vector Migration

As an alternative to the general full reverse-time approach, we have developed a significantly faster ray-based vector version.

For each point in image space, combining the wave-field polarization measured by the 3C receiver, with the space-time relationship offered by the wave equation, we generate complete estimates of both the source field and the scattered field over a reasonably large section of space surrounding the data acquisition site. Correlating or deconvolving the "scattered" wave field by the "source" wave field is the conditioning that converts the map of scattering times to a map of changes in acoustic impedance, the seismic image.

The illustration in Figure 2 shows schematically the elastic components of the scattered wave field as recorded by the 3C receivers in a VSP tool (slightly modified from Haldorsen et al. (2013)). The compressional component (f^P), the vertical shear (f^{Sv}), and the horizontal shear (f^{Sh}), present at the scattering point $\mathbf{x}$, are recorded a time $t_n(\mathbf{x}, \mathbf{x}_n)$ later at receiver n at location $\mathbf{x}_n$. These wave fields can be written:

$$\begin{aligned} f^P(\omega;\mathbf{x})e^{-i\omega t^P(\mathbf{x},\mathbf{x}_n)} &= \mathbf{p}_n^P \cdot \mathbf{d}_n(\omega) \\ f^{Sv}(\omega;\mathbf{x})e^{-i\omega t^{Sv}(\mathbf{x},\mathbf{x}_n)} &= [\mathbf{p}_n^{Sv} \times \mathbf{d}_n(\omega)]_T \\ f^{Sh}(\omega;\mathbf{x})e^{-i\omega t^{Sh}(\mathbf{x},\mathbf{x}_n)} &= [\mathbf{p}_n^{Sh} \times \mathbf{d}_n(\omega)]_V \end{aligned} \tag{5}$$

Here the vector $\mathbf{d}_n$ is the data (3C) vector, the vector $\mathbf{p}_n$ is the ray vector pointing in the direction of propagation from $\mathbf{x}$ to $\mathbf{x}_n$ for the different elastic wave-field components. The suffix T indicates a transverse component, and the suffix V indicates the component in the sagittal plane. The scattered P is polarized along the ray vector, the scattered Sv and Sh

are polarized perpendicular to the ray - and all are (mostly) mutually orthogonal.

The ray-based 3D vector migration process is essentially a 3-stage process where we for any point $\mathbf{x}_s$ in image space:

1. Propagate the source function $f^P(\omega, \mathbf{x}_0)$ forward through the source-side velocity model from the source location $\mathbf{x}_0$ to the scattering point $\mathbf{x}_s$ (for economy of arguments, we are replacing the Green's function for wave-field propagation by a time-delay operator):

$$f^{Ps}(\omega; \mathbf{x}) = f^{Ps}(\omega) e^{-i\omega t(\mathbf{x}_s, \mathbf{x})}. \quad (6)$$

2. Propagate the P projection of the recorded signal backwards through the receiver-side velocity model from each receiver n located at $\mathbf{x}_n$ to the scattering point $\mathbf{x}_s$ (again replacing the Green's function by a time-advance operator):

$$f_n^P(\omega; \mathbf{x}) = \mathbf{p}_n^P \cdot \mathbf{d}_n(\omega) e^{i\omega t(\mathbf{x}, \mathbf{x}_n)}. \quad (7)$$

3. Correlate the two wave-field reconstructions in order to impose synchronicity and coherency at point $\mathbf{x}_s$ of the source-side and receiver-side estimates (i.e., $f^{Ps}(\omega, \mathbf{x}_s)$ and $f_n^P(\omega, \mathbf{x}_s)$), apply inverse Fourier transform, keeping only the $t = 0$ values (i.e., sum over ω), sum over all receivers:

$$I(\mathbf{x}) = \sum_n \sum_\omega f^{Ps\,*}(\omega; \mathbf{x}) f_n^P(\omega; \mathbf{x}). \quad (8)$$

Substituting, and re-arranging terms:

$$\begin{aligned} I(\mathbf{x}) &= \sum_{n,\omega} f^{Ps\,*}(\omega; \mathbf{x}) f_n^P(\omega; \mathbf{x}) \\ &= \sum_{n,\omega} f^{Ps\,*}(\omega) e^{i\omega t(\mathbf{x}_s, \mathbf{x})} \mathbf{p}_n^P \cdot \mathbf{d}_n(\omega) e^{i\omega t(\mathbf{x}, \mathbf{x}_n)} \\ &= \sum_{n,\omega} \mathbf{p}_n^P \cdot [f^{Ps\,*}(\omega) \mathbf{d}_n(\omega)] e^{i\omega [t(\mathbf{x}_s, \mathbf{x}) + t(\mathbf{x}, \mathbf{x}_n)]}. \end{aligned} \quad (9)$$

In correspondence to the semblance-weighted deconvolution algorithm discussed above, for better resolution, Haldorsen et al. (2013), replace the correlation in equation 9 by one that is weighted inversely with the total energy $E_n(\omega)$ for trace n:

$$I(\mathbf{x}) = \sum_{n,\omega} \mathbf{p}_n^P \cdot [\frac{f^{Ps\,*}(\omega)}{E_n(\omega)} \mathbf{d}_n(\omega)] e^{i\omega [t(\mathbf{x}_s, \mathbf{x}) + t(\mathbf{x}, \mathbf{x}_n)]}. \quad (10)$$

Equations 9 and 10, both describe Kirchhoff-style migration sums, where we sum the (weighted) correlation between the source wave field and projections of the recorded data vector on to the ray vector at each receiver, delayed by the total travel time from the source to the receiver and stacked over frequencies and receivers.

For economy of arguments, we have ignored the parts of the Green's wave-field propagators that relate to amplitude alterations, such as absorption, spherical spreading, and accumulation of internal multiples. For the image, represented by equation 10, to be an unbiased estimate of the scattering potential of a target structure, one does need to assure that the structure is illuminated evenly. To correct for an uneven target illumination, we use the Jacobian terms described by Miller et al. (1987). Their derivation of these terms, based on the Generalized Radon Transform (GRT), gives weights that relate the distribution of sources and receivers to the energy flux density at the scattering point. With the GRT Jacobian weights and spherical spreading corrections included, we use equation 10 for fast, ray-based vector imaging of VSP data. From equations 5, one can derive expressions similar to equation 10, relating different wave-field projections to estimates of different components of the scattering potential. With appropriate velocity models, we thus may create images from refractions, transmissions, reflections, and conversions.

It should be clearly noted that this very simplified formalism blatantly ignores changes in the source signature as it accumulates a transmission response from the formation, such as interbed multiples. However, in VSP processing, the source signature is normally estimated from the down-going signal, like in equations 2 and 3. These estimates include the propagation effects, and tend to work well for imaging near the well (e.g., using equation 10), but because the ray path changes, estimates of the source signal from the down-going waves gets progressively worse as one moves away from the well. As the formation model improves, using forward modeling to estimate the source signature should improve.

An added advantage to this procedure is that it works on the total wave field, and we should not apply a pre-migration method for separating compressional and shear wave fields. The wave-field separation is all done inside the migration kernel where the geometry, the travel times, and the polarization of the propagating wave field are fully controlled. Treating the recorded 3C data as a representation of a propagating vector wave field, we create an image with a finite aperture both in plan view and in side view from single-offset data, and with the weights discussed above, we accumulate a 3D image from an ensemble of single-offset data subsets.

With the receiver outside and along the salt/sediment interface, and the specific objective to locate the salt interface, one may use different velocity models for the source propagation forward in time and the receiver propagation backwards in time. The source velocity model would contain a salt body that extends indefinitely, and the receiver velocity model will have no salt at all, just the local sediment velocities.

SYNTHETIC DATA

The imaging method will be demonstrated on a synthetic dataset generated over a complicated set of salt structures with sediments filling the space left between the salt bodies. We were given an approximate velocity model for the sediments, synthetic compressional sonic logs in two wells, and the top of the salt (the top of the salt was presumed to be well-determined from surface-seismic data).

The acquisition geometry is shown in Figure 3. Although the data had been generated with the salt in place, the velocity model we had been given had been extrapolated through the space where the salt had been, and our first objective was to determine the structure of the salt, and then the geometry of the

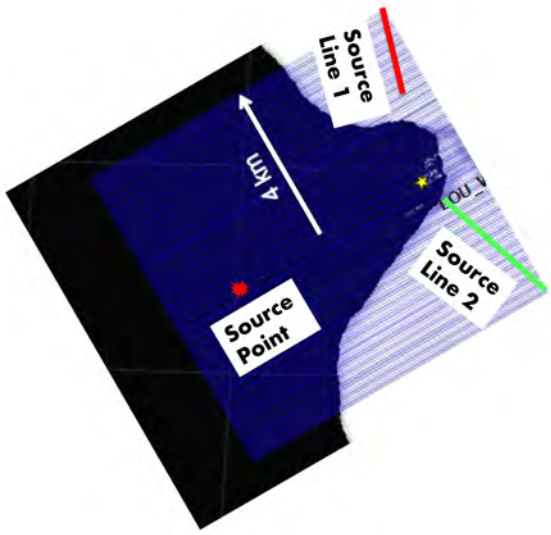

Figure 3: The aperture of the synthetic data with the top of the salt indicated by the light background color. The blue lines indicate shot lines in a 8-by-8 km grid at 30-by-40 m interval, each line from SSE to NNW. The yellow marker shows the location of the wellhead, the red marker indicates the source location for the example shot shown in Figure 4, the red and green lines show the locations of the 33 shot points along Line 1, and the 41 shot points along Line 2, used with refraction imaging to generate the image of the steeply dipping salt flank in Figure 5.

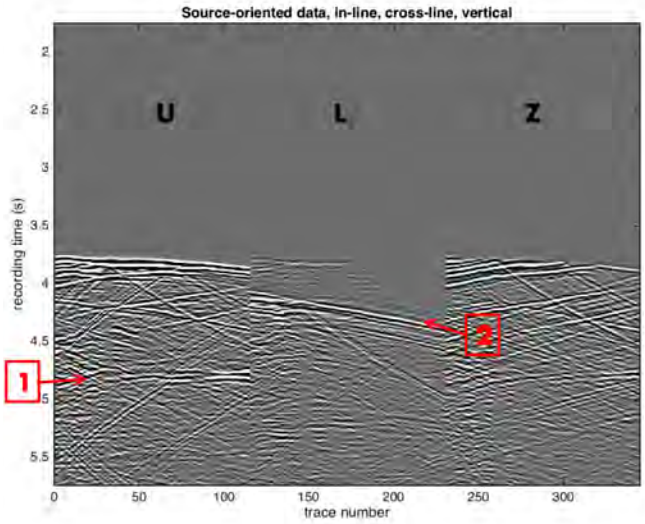

Figure 4: Three-component data acquired at the shot point indicated with a red marker in Figure 3, a little more than 5.6 km away from the nearest and 5.9 km away from the furthest receiver. The data have been oriented in source-receiver sagittal plane (U), a direction perpendicular to this (L), and a vertical direction (Z). We have annotated two wave-field components of particular interest by the numbers 1 and 2. These are discussed in the text.

sediments under the salt canopy.

Figure 4 shows data acquired at a shot point indicated with a red asterisk in Figure 3, a little more than 5.6 km WSW from the well. On the display in Figure 4, we have annotated two wave-field components of particular interest:

1. A component appearing mostly on the in-line geophone, and weakly on the vertical geophone in the deepest part of the well. With a move-out mostly parallel to the first arrival, this is a candidate for a compressional reflection back to the well from an interface straight ahead in the source-receiver sagittal plane, about a kilometer away, with a dip nearly parallel to the slightly deviated well.

2. A component appearing on all three geophones, with a maximum amplitude at azimuths between 35° and 45°, counter-clock wise from the source-receiver sagittal plane. This is a candidate for a compressional reflection from the salt body on the right looking from the shot point towards the well.

As with the general method - and assuming that we do not know where the interface between the salt and the sediments are - the source-side forward-projection and the receiver-side back-projection can be performed in two separate velocity models. We can use this formalism in a 2D setting to image the salt flank and the bordering sediments (Brooks et al. (2015); Haldorsen et al. (2015)).

In Figure 5, we show the image of the steeply dipping salt/sediment interface obtained underneath the salt overhang by assuming that the compressional waves are refracted on exiting the salt. We used the shot points along the red and green lines indicated on Figure 3, extending from the furthest North and East corners of the acquisition aperture, towards the well. The receiver-side travel times, after the refraction, were calculated through the sediment sagittal-plane velocity models, and the source-side travel times from models where the salt velocity had been substituted at depth greater than the top of the salt.

A wave-field component that is generated by a shot outside the salt, and then reflected at the salt-sediment boundary towards the receivers, will never enter the salt. This means that we can use a velocity model containing only sediments for both the source-side and the receiver-side ray tracing. A full 3D vector migration using a velocity model with no salt should thus give a definite answer for where the wave-field components pointed to in Figure 4 are coming from. In other words, we should not need to know where the salt is in order to generate a good image of salt-sediment interface. We do require a good velocity model for the sediments, and we should be aware of that components of the image beyond the edge of the salt will be miss-located. For the migration, we were very careful only to use shot points where the source was located well outside the top of the salt indicated on Figure 3.

In Figure 6, we show a comparison of the true model with a vertical section reflection image of the sediments obtained from using only sediment velocities from the true model, and the shots on the outside of the salt. Figure 7 shows a horizontal section through the image at a depth of around 2600m, and

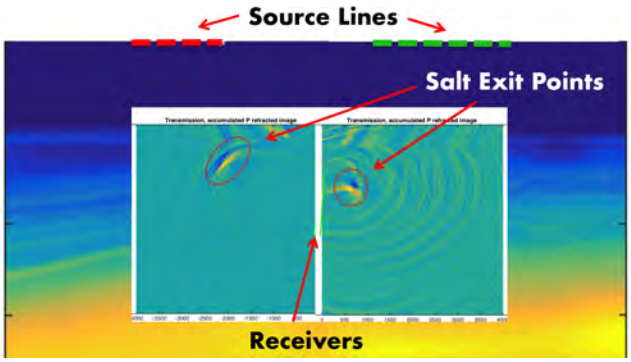

Figure 5: Map of salt/sediment refraction points underneath the overhanging salt, superimposed on the "sediment" velocity model. The 2D images are obtained from the shots along the red and green lines in Figure 3, assuming that the compressional waves are refracted on exiting the salt. The green line indicates the nearly 1.5 km long receiver array. The underside of the salt is at a depth of around 2.5 km, at offsets of about 2 and 0.5 km from the receiver array.

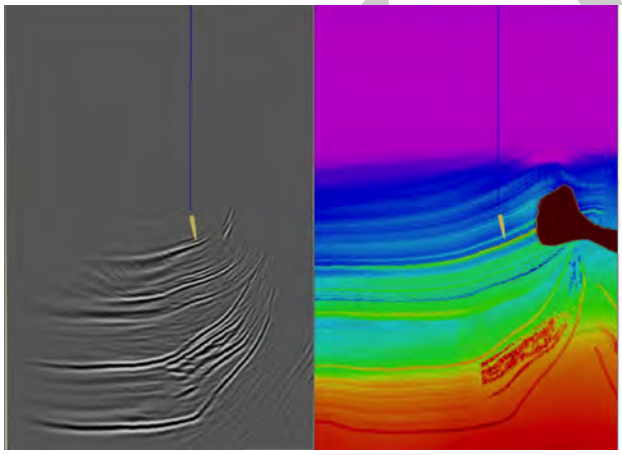

Figure 6: On the left: a vertical section through the reflection image of the sediments, obtained from using only sediment velocities from the true model, and the shots on the outside of the salt. On the right: the true model.

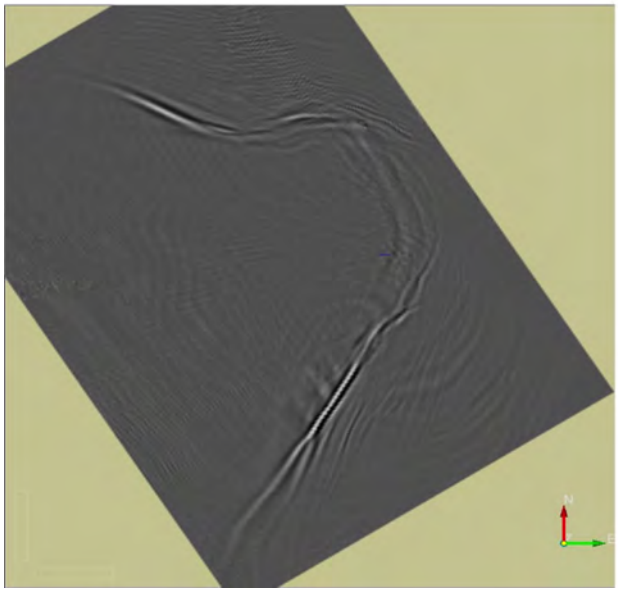

Figure 7: A horizontal section through the 3D image cube at a depth of 2820 m, showing the outline of the salt at this depth. Whereas the aperture of the data is 8-by-8 km, the aperture of the image is 4-by-5 km. Only sediment velocities are used for this image, and taking care to eliminate the shots propagating through the salt.

Figure 8 shows a section from the North-West to the South-East, through the two major salt bodies. The salt/sediment stands out as a singular, very strong event. This event was picked on all depth sections, resulting in the 3D interface surrounding the well, as shown in Figure 9. The interface tilts away from the well as we got to greater depths.

For all images shown in Figures 6, 7, and 8, we used the same sediments-only velocity model, taking care to eliminate the shots generating rays through the salt. However, looking for the sediments, we used scattering angles from 0° to 120°, and looking for the salt interfaces, we used scattering angles ranging from 90° to 180°, i.e., only down-scattered rays.

In the final processing of the data, we use this information to place the salt into the velocity model and the 3D vector migration with the complete and updated velocity model to generate images of the sedimentary layers under the salt canopy and up against the salt.

CONCLUSIONS

The salt body has successfully been delineated in three dimensions using an approach based on 3D vector migration, applying a fast, ray-based migration to data acquired with three-component down-hole receivers.

ACKNOWLEDGEMENTS

We thank Total SA, and READ AS for permission to show this work and allocate the resources required to obtain these results.

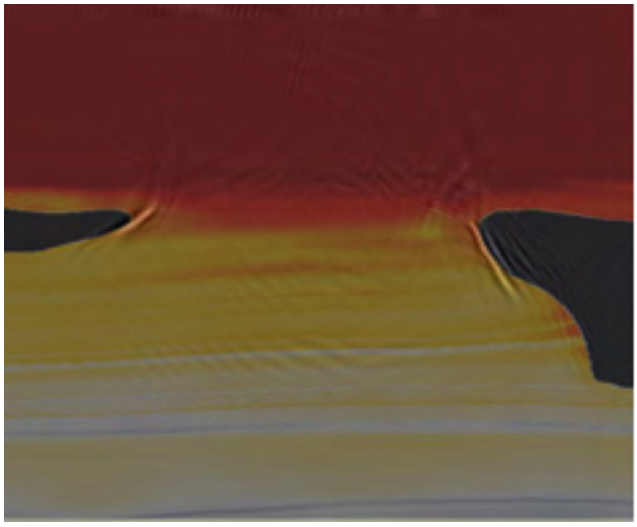

Figure 8: A vertical section through the 3D image cube from the North-West to the South-East, intersection the two main salt bodies, overlain by the true velocity model. The salt bodies are the two dark-grey objects to the left and to the right. Only sediment velocities are used for this image, and taking care to eliminate the shots propagating through the salt.

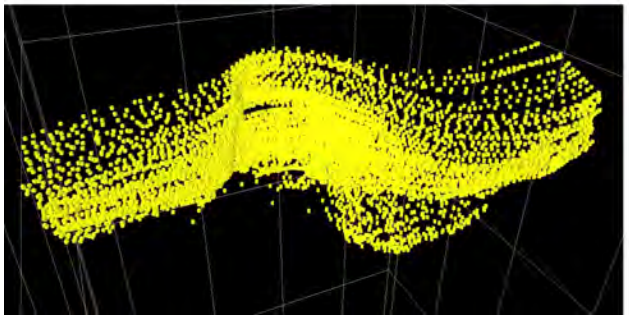

Figure 9: The 3D salt/sediment interface surrounding the well, as interpreted from the vector migrated image cube.

REFERENCES

Aki and Richard, 2009, Quantitative Seismology, 2nd edition: University Science Books.

Brooks, N. J., P. Donais, W. Heigl, J. Haldorsen, and F. Li, 2015, Defining a steeply dipping salt flank in Mississippi with a new high-certainty 3-D method: Gulf Coast Association of Geological Societies 65th Annual Convention, Extended Abstracts.

Claerbout, J. F., 1985, Imaging the Earth's Interior: Blackwell Science Inc.

Gerea, C., P.-L. Pichon, G. Geddes, M. Verliac, V. Lesnikov, 2016, Proficient Subsalt Monitoring with 3D Well Seismic, deep-offshore West Africa: 86th SEG Annual Meeting and International Exposition

Gillespie, R. H., 1995, Rise of the Texas oil industry: Part 1: Exploration at Spindletop: SEG The Leading Edge, Vol. 14, No. 1, pp. 22-24.

Haldorsen, J. B. U., 2002, Converted-shear and compressional images using Projection Imaging: The 64th EAGE Conference and Exhibition, Extended Abstracts, Paper F031.

Haldorsen, J., N. Brooks, P. Donais, W. Heigl, F. Li, 2015, A Migration Approach to Generating Continuous Images of Salt and Sediment Boundaries from Multi-Offset VSP Data: Fourteenth International Congress of the Brazilian Geophysical Society, Rio de Janeiro, Brazil, August 2015.

Haldorsen, J. B.U., T. Hilton, M. Milenkovic, M., C. Schinelli, L. F. Soares, J. E. Lira, A. Zelia, 2013, Formation Imaging from Three-Component Borehole-Seismic Data Using both Space-time Relations and Wave-Field Polarization: Thirteenth International Congress of the Brazilian Geophysical Society, Rio de Janeiro, Brazil, August 2013.

Haldorsen, J., D. Miller, J. Walsh, 1994, Multichannel Wiener Deconvolution of Vertical Seismic Profiles, Geophysics, 59, 10, pp. 1500-1511.

Lou, M., D. Cheng, and F. Doherty, 2012, 3D anisotropic calculation of salt-face exit point for VSP salt proximity surveys: SEG Technical Program Expanded Abstracts 2012: 1-5.